

# AI-Limited Fluid Antenna-Aided Integrated Sensing and Communication Systems

Farshad Rostami Ghadi, Member, IEEE, Kai-Kit Wong, Fellow, IEEE,  
 F. Javier López-Martínez, Senior Member, IEEE, Zhentian Zhang, Graduate Student Member, IEEE,  
 Hyundong Shin, Fellow, IEEE, and Christos Masouros, Fellow, IEEE

**Abstract**—This paper characterizes the fundamental limits of integrated sensing and communication (ISAC) when the transmitter is subject to an artificial intelligence (AI) representation bottleneck and the receiver employs a fluid antenna system (FAS). Specifically, the message is first encoded into an ideal Gaussian waveform and mapped by an AI encoder into a finite-capacity latent representation that constitutes the physical channel input, while the FAS receiver selects the port experiencing the most favorable channel conditions. We reveal that the AI bottleneck is equivalent to an additive representation noise, which reduces both the communication and sensing signal-to-noise ratios (SNRs) at the selected port. We then derive the resulting ISAC capacity-distortion region and establish tight converse and achievability bounds under general fading models, including Jakes-correlated channels. Leveraging the spatial degrees of freedom (DoF) characterization of the Jakes' model, we furthermore prove that the port-selection gain is fundamentally constrained by the physical length of the FAS region: the effective diversity order equals the numerical rank of the Jakes' correlation matrix and increases only with the FAS length. Consequently, enlarging the FAS length allows the selected-port SNR to approach the AI-imposed ceiling, driving

The work of F. Rostami Ghadi is supported by the European Union's Horizon 2022 Research and Innovation Programme under Marie Skłodowska-Curie Grant No. 101107993.

The work of K. K. Wong is supported by the Engineering and Physical Sciences Research Council (EPSRC) under Grant EP/W026813/1.

The work of F. J. López-Martínez is supported by grant PID2023-149975OB-I00 (COSTUME) funded by MICIU/AEI/10.13039/501100011033, and by ERDF/EU.

The work of H. Shin is supported by the National Research Foundation of Korea (NRF) grant funded by the Korean government (MSIT) (RS-2025-00556064 and RS-2025-25442355), and by the Ministry of Science and ICT (MSIT), Korea, under the ITRC (Information Technology Research Center) support program (IITP-2025-RS-2021-II212046), supervised by the IITP (Institute for Information & Communications Technology Planning & Evaluation).

F. Rostami Ghadi and F. J. López-Martínez are with the Department of Signal Theory, Networking and Communications, Research Centre for Information and Communication Technologies (CITIC-UGR), University of Granada, 18071, Granada, Spain (e-mail: {f.rostami, fjlsm}@ugr.es).

K. K. Wong is with the Department of Electronic and Electrical Engineering, University College London, WC1E 7JE, London, United Kingdom, and also with the Department of Electronic Engineering, Kyung Hee University, Yongin-si, Gyeonggi-do 17104, Republic of Korea (e-mail: kai-kit.wong@ucl.ac.uk).

Z. Zhang is with the National Mobile Communications Research Laboratory, Southeast University, Nanjing, 210096, China (e-mail: zhentianzhangzzt@gmail.com).

H. Shin is with the Department of Electronics and Information Convergence Engineering, Kyung Hee University, Yongin-si, Gyeonggi-do 17104, Republic of Korea (e-mail: hshin@khu.ac.kr).

C. Masouros is with the Department of Electronic and Electrical Engineering, University College London, WC1E 7JE, London, United Kingdom (e-mail: c.masouros@ucl.ac.uk).

Corresponding Author: Farshad Rostami Ghadi.

the achievable communication rate and sensing mean-square error (MSE) toward their AI-limited fundamental bounds. Numerical results corroborate the analysis and scaling laws.

**Index Terms**—Integrated sensing and communication (ISAC), fluid antenna system (FAS), information bottleneck, AI.

## I. Introduction

### A. Context

INTEGRATED sensing and communication (ISAC) being a core capability for sixth-generation (6G) mobile networks, facilitates simultaneous data transmission and environmental perception within a unified physical layer [1], [2]. Most existing analyses of ISAC, nevertheless, assume ideal transceiver processing in which signals can be represented and manipulated with unlimited precision. In practice, modern transceivers increasingly rely on artificial intelligence (AI)-based modules such as neural encoders and feature extractors.

These modules possess finite representational capacity and cannot preserve all information contained in the ideal baseband signal. This limitation can be naturally modeled as a learning or representation bottleneck in the transmit chain, whereby each symbol must be compressed into a latent variable with restricted information content [3]. Such an AI-induced bottleneck fundamentally alters the effective signal quality seen by both communication and sensing receivers and introduces new performance ceilings that are absent in classical ISAC models.

A defining characteristic of ISAC systems is the intrinsic trade-off between communication and sensing performance, as both functions share common physical resources such as power, bandwidth, and waveform degrees of freedom (DoF). Enhancing communication reliability normally would reduce the fidelity of sensing observations, while prioritizing sensing accuracy can limit the achievable rate. These conflicting goals have motivated extensive information-theoretic studies of ISAC capacity-distortion trade-offs, which characterize the fundamental limits of jointly transmitting information while estimating environmental parameters. However, most existing results rely on ideal waveform generation and signal representation assumptions, and hence do not capture the impact of practical AI-driven transceiver constraints. When waveform generation is subjected to a finite-capacity AI representation bottleneck, the classical ISAC trade-off is

fundamentally reshaped; even under favorable channel conditions, the achievable communication rate and sensing accuracy are bounded by the information that can be preserved through the AI module.

On the other hand, fluid antenna systems (FAS) have recently emerged as a practical and highly versatile alternative to conventional fixed-antenna architectures [4]. By dynamically exposing one of many closely spaced ports on a single radio frequency (RF) chain, a port selection-based FAS is able to finely sample the spatial channel at multiple locations within a compact physical space. More precisely, FAS is a hardware-agnostic system concept that treats the antenna as an adaptable physical-layer resource to broaden system design and network optimization [5], [6], [7], [8]. In [9], Lu et al. provided an explanation to FAS through the lens of electromagnetic. FAS in practice can take many different forms, including movable elements [10], liquid-based antennas [11], [12], metamaterials [13], [14], [15], reconfigurable pixels [16], [17], [18] and etc. In [19], Tong et al. discussed the pros and cons of different implementation technologies for realizing the FAS concept.

The capability of FAS provides several advantages that are attractive for ISAC. First of all, port selection exploits location-dependent channel variations, yielding diversity gains akin to multi-antenna systems but without the associated complexity. Second, selecting the strongest among many spatially distinct channel realizations creates an inherent gain that can significantly enhance both communication reliability and sensing sensitivity. Third, the fine spatial granularity of FAS enables improved electromagnetic sampling of the environment, which is especially beneficial for sensing tasks in which small spatial displacements induce meaningful variations in reflected signals [20], [21], [22], [24]. These properties make FAS a promising architecture for mitigating the degradation induced by AI representation bottlenecks and recovering ISAC performance that would otherwise be lost due to finite learning capacity.

## B. State-of-the-Art

In recent years, the information-theoretic and AI-enabled aspects of ISAC and FAS have been separately studied. For instance, the exact capacity-distortion region of single-receiver Gaussian ISAC was established in [25], and later extended to collaborative multiuser networks in [26]. Finite-blocklength ISAC performance was analyzed in [27], while [28] introduced log-loss sensing mutual information (MI) as a unified metric for joint communication-sensing system design. On the other hand, the rate-Cramér-Rao bound (CRB) region for multiple-input multiple-output (MIMO) ISAC was investigated in [29], while [30], [31] analyzed rate-detection and rate-CRB trade-offs in dual-functional radar/communication systems. Besides, surveys such as [33] and [32] have documented the growing role of deep learning in waveform design, target estimation, and adaptive beamforming. Additionally, learning-based ISAC architectures including

federated and fog-enabled implementations [34] and deep joint waveform-beamforming designs [35] demonstrate significant empirical gains. Also, the information bottleneck framework [36] and its deep variational extensions [37] provide mechanisms to regulate the MI carried by latent representations. Deep task-based quantization and bit-limited radar/communication have also been explored in [38], [39].

Meanwhile, the information-theoretic limits of MIMO-FAS were recently characterized in [40], demonstrating superior diversity-multiplexing behavior and improved  $q$ -outage capacity relative to the classical MIMO system. FAS-assisted dirty multiple access channels were analyzed in [41], where spatial correlation was captured accurately using copula theory and sizable outage gains were reported. In the context of multiuser information-theoretic analysis, fluid antenna multiple access (FAMA) has also been investigated under strong interference channels in [42], where combining FAS-enabled spatial reconfigurability with simultaneous non-unique decoding has been shown to markedly improve the system performance.

Several learning-based approaches such as deep reinforcement learning for ISAC precoding with planar FAS [43], deep learning-enabled FAMA [44], and fast port selection methods [45], demonstrate the synergy between FAS reconfigurability and data-driven design. More recently, opportunistic multiuser FAMA via team-theoretic reinforcement learning was further developed in [46], and active sensing-based beam alignment for MIMO-FAS was also proposed in [47].

## C. Motivation and Contributions

Despite the aforesaid advantages of both ISAC and FAS, the interplay between FAS-assisted ISAC systems and AI-limited models is not understood. Existing studies on AI-constrained ISAC primarily consider conventional fixed-antenna architectures, e.g., MIMO, and therefore do not capture the spatial sampling and selection dynamics introduced by FAS. Likewise, the current FAS literature focuses largely upon communication performance metrics such as outage probability and diversity gain, without incorporating learning constraints and sensing accuracy. Consequently, the fundamental limits of ISAC systems that operate under both AI representation constraints and FAS-based port selection remain unknown.

Motivated by this, this work provides the first information-theoretic characterization of FAS-assisted ISAC systems that operate under a pre-channel AI representation constraint. The main contributions are summarized as follows.

- AI-constrained FAS-assisted ISAC. We develop a unified model where each ideal transmit symbol is compressed into a latent representation of limited information content, while the FAS receiver selects one optimal port for joint communication and sensing. This structure induces the Markov relationship between the ideal symbol, its AI-generated representation, and the received communication and sensing

observations, and it embeds the port selection process through the selected channel gains.

- **Capacity-distortion characterization.** For Gaussian representations, we show that the AI bottleneck with a FAS receiver manifests as an additional effective noise term that degrades both communication and sensing performance at the selected port. Using this equivalence, we derive explicit expressions for the achievable communication rate and sensing mean square distortion as functions of the FAS-selected channel gains. Furthermore, we establish matching converse and achievability bounds, thereby providing a complete description of the ISAC capacity-distortion region under the Rayleigh fading model.
- **FAS spatial DoF.** Under rich scattering with the Jakes' correlation model, we characterize the effective spatial DoF of the FAS in the proposed AI-limited ISAC system and show that the port selection gain is fundamentally limited by the physical length of the FAS region. The resulting diversity order equals the numerical rank of the Jakes correlation matrix and increases only with the FAS length, irrespective of the number of available ports.
- **AI-limited performance ceiling.** Additionally, we reveal that enlarging the FAS length enables the selected port signal-to-noise ratio (SNR) to approach the AI-imposed ceiling, allowing both the achievable communication rate and sensing distortion to converge to their AI-limited fundamental bounds. Numerical results validate the theoretical analysis and illustrate the trade-offs between AI capacity, spatial diversity, and ISAC performance.

#### D. Organization and Mathematical Notations

The remainder of this paper is organized as follows. Section II introduces the system model, including the pre-channel AI representation bottleneck, the FAS receive architecture, and the adopted performance metrics. Section III derives the capacity-distortion region of the proposed AI-constrained FAS-enabled ISAC system and establishes matching converse and achievability bounds. Section IV characterizes the statistics of the FAS-selected port gains under spatially correlated fading and analyzes the finite port performance. Section V investigates the asymptotic behavior with respect to the physical length of the fluid antenna, revealing the role of spatial DoF in compensating the AI bottleneck. Section VI presents a practical variational information bottleneck (VIB) encoder design that realizes the theoretical Gaussian representation model. Section VII provides numerical results that validate the analysis and illustrate key trade-offs. Finally, Section VIII concludes the paper and discusses future research directions.

Throughout the paper, scalar variables are denoted by lowercase letters  $x$ , vectors by boldface lowercase letters  $\mathbf{x}$ , and matrices by boldface uppercase letters  $\mathbf{X}$ . The superscripts  $(\cdot)^\top$  and  $(\cdot)^\dagger$  denote transpose and Hermitian transpose, respectively. The operators  $\mathbb{E}[\cdot]$  and  $\mathbb{P}(\cdot)$

TABLE I  
Summary of Notations

Symbol	Description
$M$	Transmit information message
$X$	Ideal transmitted symbol
$Z$	Latent representation
$W_z$	AI representation noise
$C_{\text{AI}}$	AI representation capacity
$N_z$	Representation noise variance
$N_z^*$	Representation noise minimum value
$P$	Transmit power
$N_0$	Thermal noise variance
$Y_c$	Communication received signal
$Y_c, Y_s$	Sensing received signal
$\theta$	Random sensing parameter of interest
$\sigma_\theta^2$	Variance of the sensing parameter
$h_{c,\ell}$	Communication channel gain at port $\ell$
$h_{s,\ell}$	Sensing channel gain at port $\ell$
$\mathbf{h}_c$	Communication channel vector
$\mathbf{h}_s$	Sensing channel vector
$\ell^*$	Selected FAS port index
$U(\cdot)$	Utility function used for port selection
$L$	Number of FAS ports
$W$	Physical length of the fluid antenna
$d$	Inter-port spacing in the FAS
$\lambda$	Carrier wavelength
$\mathbf{R}$	Spatial correlation matrix of the FAS channels
$\gamma_s^*$	Selected port communication gain
$\gamma_s^*$	Selected port sensing gain
$\Gamma_c^*$	Effective communication SNR
$\Gamma_s^*$	Effective sensing SNR
$\Gamma_{\text{AI}}$	AI-imposed SNR ceiling
$L'(W)$	Effective number of spatial DoF
$R$	Achievable communication rate
$D_s$	Sensing distortion

denote statistical expectation and probability. The notation  $\mathcal{CN}(0, \sigma^2)$  represents a circularly symmetric complex Gaussian random variable with zero mean and variance  $\sigma^2$ . Also, MI is measured in bits and denoted by  $I(\cdot; \cdot)$ . The notation  $\arg \max$  returns the maximizing index. The symbol  $o(\cdot)$  follows standard asymptotic notation. Unless otherwise stated,  $\log(\cdot)$  represents the base-2 logarithm. For convenience, the main symbols and variables used throughout the paper are summarized in Table I.

## II. System Model

As illustrated in Fig. 1, we consider an ISAC system where the transmitter seeks to convey a message  $M$  to a FAS-equipped ISAC receiver that jointly performs communication decoding and sensing estimation, using  $L$  closely spaced ports, while simultaneously enabling the estimation of a random sensing parameter  $\theta$ , e.g., target delay, reflection coefficient. The message  $M$  is encoded into a length- $n$  codeword  $\{X_t\}_{t=1}^n$  with independent and identically distributed (i.i.d.) Gaussian components  $X_t \sim \mathcal{CN}(0, P)$ , which is an information-theoretic abstraction to characterize fundamental performance limits. However, the symbol that actually enters the physical channel is not

$X_t$  itself but a latent representation  $Z_t$  produced by an AI encoder subject to a finite AI representation-capacity (learning) constraint, which limits the MI between the ideal transmitted symbol and its latent representation, rather than the physical communication channel capacity.

### A. Pre-Channel AI Representation Bottleneck

The AI encoder implements a memoryless stochastic mapping from the ideal symbol  $X$  to a latent representation  $Z$  under a prescribed information budget. Formally, the mapping is described by a conditional distribution  $p(z|x)$  that must satisfy an MI constraint

$$I(X; Z) \leq C_{\text{AI}}, \quad (1)$$

where  $C_{\text{AI}}$  quantifies the maximum number of relevant bits that the learning module can retain from the ideal transmit symbol [48], [49].

Following standard information bottleneck formulations, we adopt a Gaussian representation model

$$Z = X + W_z, \text{ where } W_z \sim \mathcal{CN}(0, N_z), \quad (2)$$

with  $W_z$  independent of  $X$ , where  $W_z$  is a zero-mean circularly symmetric complex Gaussian representation noise term and  $N_z$  is its variance. For this model, the MI satisfies

$$I(X; Z) = \log_2 \left( 1 + \frac{P}{N_z} \right), \quad (3)$$

where  $P$  is the transmit power.

Enforcing (1) with equality yields the minimum feasible representation noise variance

$$N_z^* = \frac{P}{2^{C_{\text{AI}}} - 1}, \quad (4)$$

which characterizes the effective information loss introduced by the AI bottleneck. Consequently, the pre-channel AI processing manifests as an additive distortion whose impact depends on the subsequent propagation channel.

### B. FAS-Equipped Receiver Model

The FAS architecture affects the system exclusively through the spatial structure of the received channel realizations and the subsequent port selection rule, while the underlying physical ISAC channel law remains unchanged. The ISAC receiver, which jointly decodes the transmitted data message and estimates the sensing parameter, is equipped with a fluid antenna exposing a set of  $L$  ports indexed by  $\ell \in \{1, \dots, L\}$ . These ports correspond to distinct physical locations, enabling the ISAC receiver to exploit small-scale spatial variations in the propagation environment for both communication and sensing tasks. At each channel use, the receiver selects a single port according to a deterministic selection rule

$$\ell^* = \arg \max_{\ell} U(h_{c,\ell}, h_{s,\ell}), \quad (5)$$

in which  $h_{c,\ell}$  and  $h_{s,\ell}$  denote the communication and sensing channel gains at port  $\ell$ , respectively, and  $U(\cdot)$

denotes the utility function used for port selection. Here, for simplicity, we have taken  $U = |h_{c,\ell}|^2$ . Therefore, given the latent channel input  $Z$ , the per-port received signals are given by

$$Y_{c,\ell} = h_{c,\ell}Z + N_c \quad (6)$$

and

$$Y_{s,\ell} = h_{s,\ell}(\theta)Z + N_s, \quad (7)$$

where  $h_{s,\ell}(\theta)$  captures the dependence of the sensing channel on the unknown parameter  $\theta$ , and noise terms  $N_c$  and  $N_s$  are independent circularly symmetric complex Gaussian random variables with variance  $N_0$ .

Substituting the AI representation model (2) into the above expressions yields the effective per-port models

$$Y_{c,\ell} = h_{c,\ell}X + \underbrace{h_{c,\ell}W_z + N_c}_{\hat{N}_{c,\ell}} \quad (8)$$

and

$$Y_{s,\ell} = h_{s,\ell}(\theta)X + \underbrace{h_{s,\ell}(\theta)W_z + N_s}_{\hat{N}_{s,\ell}}. \quad (9)$$

The equivalent noise terms  $\hat{N}_{c,\ell}$  and  $\hat{N}_{s,\ell}$  remain Gaussian due to linearity and independence such that their corresponding variances can be found as

$$\sigma_{c,\ell}^2 = N_0 + |h_{c,\ell}|^2 N_z^* \quad (10)$$

and

$$\sigma_{s,\ell}^2 = N_0 + |h_{s,\ell}(\theta)|^2 N_z^*. \quad (11)$$

Thus, the effective communication and sensing SNRs at port  $\ell$ , respectively, become

$$\Gamma_{c,\ell} = \frac{|h_{c,\ell}|^2 P}{N_0 + |h_{c,\ell}|^2 N_z^*} \quad (12)$$

and

$$\Gamma_{s,\ell} = \frac{|h_{s,\ell}(\theta)|^2 P}{N_0 + |h_{s,\ell}(\theta)|^2 N_z^*}. \quad (13)$$

Under the port selection rule (5), the system operates with random selected port gains  $H_c^* = h_{c,\ell^*}$  and  $H_s^* = h_{s,\ell^*}$ , and the corresponding effective SNRs,  $\Gamma_c^*$  and  $\Gamma_s^*$ .

### C. Performance Metrics

ISAC performance is characterized in terms of both communication reliability and sensing accuracy. Let  $\mathcal{M}$  be the message set and  $\hat{M}$  be the message estimate produced by the communication receiver after observing  $Y_{c,\ell^*}^n$  over  $n$  channel uses. Therefore, the communication rate is defined as

$$R = \frac{1}{n} \log_2 |\mathcal{M}|, \quad (14)$$

and a rate  $R$  is said to be achievable if the decoding error probability satisfies  $\mathbb{P}(\hat{M} \neq M) \rightarrow 0$  as  $n \rightarrow \infty$ .

For sensing, the receiver forms an estimate  $\hat{\theta}$  of the underlying parameter  $\theta$  using the sequence of sensing

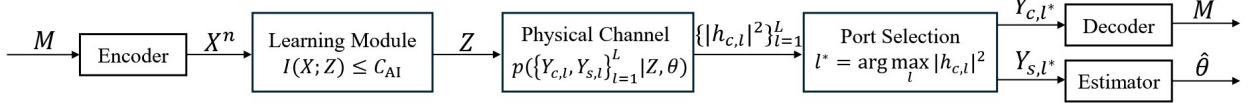


Fig. 1. Information-theoretic abstraction of the AI-constrained FAS-aided ISAC system model.

observations  $Y_{s,\ell^*}^n$ . We measure sensing performance by the mean square error (MSE), defined as

$$D_s = \mathbb{E} \left[ \left| \theta - \hat{\theta}(Y_{s,\ell^*}^n) \right|^2 \right], \quad (15)$$

in which a distortion level  $D_s$  is achievable if there exists an estimator such that the above MSE is attained in the limit of large blocklength.

Note that the fundamental trade-off between communication and sensing under the AI representation constraint is captured by the capacity-distortion region, denoted as  $\mathcal{R}_{\text{AI-FAS}}(C_{\text{AI}})$ , which consists of all pairs  $(R, D_s)$  that are simultaneously achievable when the input representation mapping is constrained to meet  $I(X; Z) \leq C_{\text{AI}}$ . This region characterizes the optimal performance limits of ISAC with an AI-constrained transmitter and an FAS-enabled receiver.

### III. Capacity-Distortion Region

This section establishes the fundamental communication-sensing trade-off for the considered ISAC architecture with an AI-constrained transmitter and an FAS-enabled receiver. The analysis captures, in closed-form, how the AI representation bottleneck and the selected port gains jointly determine the maximum achievable communication rate and the minimum attainable sensing distortion. The result applies to general FAS fading statistics and any deterministic port selection rule.

**Theorem 1** (Capacity-Distortion Region). Consider an ISAC system with the AI representation constraint  $I(X; Z) \leq C_{\text{AI}}$ , employing the Gaussian representation model (2), and having an FAS receiver using the selection rule in (5). The achievable communication rate  $R$  and sensing distortion  $D_s$  satisfy

$$R \leq \mathbb{E} \left[ \log_2 \left( 1 + \frac{|H_c^*|^2 P}{N_0 + |H_c^*|^2 N_z^*} \right) \right] \quad (16)$$

and

$$D_s \geq \mathbb{E} \left[ \frac{\sigma_\theta^2}{1 + \frac{|H_s^*|^2 P}{N_0 + |H_s^*|^2 N_z^*}} \right], \quad (17)$$

where  $N_z^*$  denotes the minimum representation noise variance permitted by the AI bottleneck, and the expectation is taken over the distribution of the selected port gains  $(H_c^*, H_s^*)$ . Furthermore, these bounds are tight such that every pair  $(R, D_s)$  satisfying (16)-(17) is achievable.

**Proof:** The converse follows from the Markov chain  $M \rightarrow X^n \rightarrow Z^n \rightarrow (Y_c^n, Y_s^n)$ , where the selected port observations  $(Y_{c,\ell^*}^n, Y_{s,\ell^*}^n)$  are deterministic functions of  $(Y_c^n, Y_s^n)$  and the section rule. This implies via Fano's inequality that

$$nR \leq I(Z^n; Y_{c,\ell^*}^n, l^*) + o(n). \quad (18)$$

Applying the chain rule, conditioning on the selected port, and invoking the memorylessness of the channel yield a single-letter upper bound on  $I(Z; Y_c)$  evaluated under the constraint  $I(X; Z) \leq C_{\text{AI}}$ . The Gaussian channel is optimal under this MI constraint, and substituting its equivalent representation-noise variance  $N_z^*$  produces (16).

For sensing, the minimum MSE-MI identity links the minimum achievable distortion to the information conveyed by  $Y_s$  about  $\theta$ . Evaluating this relationship for the Gaussian model and accounting for the selected port distribution yields the lower bound in (17).

Achievability is established using Gaussian codebooks for  $X^n$ , the optimal Gaussian mapping  $X^n \mapsto Z^n$ , and standard maximum-likelihood and minimum MSE estimators at the selected port. The resulting communication rate and sensing distortion attain the expressions on the right-hand sides of (16) and (17), completing the characterization. ■

Theorem 1 holds for arbitrary joint fading distributions of the port dependent channel gains  $\{(h_{c,\ell}, h_{s,\ell})\}$  and for any deterministic utility-based selection policy. In the following sections, we investigate the implications of this general region for commonly studied FAS models and characterize how the number of ports and the underlying fading statistics shape the achievable ISAC performance.

### IV. FAS Statistics and Finite- $L$ Performance

The capacity-distortion region in Theorem 1 depends on the statistics of the selected port gains  $H_c^* = h_{c,\ell^*}$  and  $H_s^* = h_{s,\ell^*}$  through  $\gamma_c^* = |H_c^*|^2$  and  $\gamma_s^* = |H_s^*|^2$ . In FAS, these gains are strongly affected by the spatial correlation among ports, where such correlation is typically characterized by Jakes' model in the case of rich scattering. Accordingly, this section explains how existing analytical results for FAS-selected port gains can be combined with the proposed AI-limited ISAC framework.

For the considered one-dimensional (1D) FAS with  $L$  ports, length  $W$ , the inter-port spacing is given by  $d = W/(L-1)$ . The communication channel vector is defined as

$$\mathbf{h}_c = (h_{c,1}, \dots, h_{c,L})^\top, \quad (19)$$

a zero-mean circularly symmetric complex Gaussian vector  $\mathbf{h}_c \sim \mathcal{CN}(\mathbf{0}, \mathbf{R})$ , with spatial covariance matrix

$$R_{k,\ell} = J_0\left(\frac{2\pi}{\lambda}|k - \ell|d\right), \quad (20)$$

where  $J_0(\cdot)$  is the zeroth-order Bessel function of the first kind and  $\lambda$  is the wavelength. The sensing channel vector  $\mathbf{h}_s = (h_{s,1}, \dots, h_{s,L})^\top$  is modeled with the same spatial scattering structure as  $\mathbf{h}_c$ , so that both channels exhibit identical Jakes's model spatial correlation across the FAS ports.

Using the SNR maximizing selection rule

$$\ell^* = \arg \max_{\ell \in \{1, \dots, L\}} |h_{c,\ell}|^2, \quad (21)$$

the selected port communication gain is defined as  $\gamma_c^* = \max_{\ell} |h_{c,\ell}|^2$ , and the sensing gain at the selected port is given by  $\gamma_s^* = |h_{s,\ell^*}|^2$ , where the corresponding distributions are derived in terms of the spatial correlation matrix  $\mathbf{R}$  in [50]. It has been proven in [50] that there exists an integer  $L'(W) \leq L$  depending only on the length  $W$  (and thus on  $\mathbf{R}$ ) such that increasing the number of ports beyond  $L'(W)$  does not yield additional diversity gain. In other words, the effective number of diversity branches of the FAS is governed by the physical length, and not by the nominal port count.

On the other hand, the sensing gain  $\gamma_s^*$  depends on how  $\mathbf{h}_s$  is correlated with  $\mathbf{h}_c$ . When  $\mathbf{h}_s$  and  $\mathbf{h}_c$  are independent and have the same marginal Rayleigh distribution, the index  $\ell^*$  in (21) is independent of  $\mathbf{h}_s$ , and thus  $\gamma_s^*$  has the same marginal distribution as  $|h_{s,\ell}|^2$ , i.e., exponential with unit mean. When communication and sensing share common scatterers,  $\gamma_s^*$  can be obtained from the joint covariance of  $(\mathbf{h}_c, \mathbf{h}_s)$  using the same methodology as in [50], but applied to an augmented block covariance matrix.

In our AI-constrained ISAC setting, the representation bottleneck introduces an additional noise term  $N_z^*$  in the effective SNRs at the selected FAS port. Specifically, for a given realization of the selected gain  $\gamma_c^*$ , the effective communication SNR is denoted as

$$\Gamma_c^* = \frac{\gamma_c^* P}{N_0 + \gamma_c^* N_z^*}, \quad (22)$$

and the sensing SNR is defined as

$$\Gamma_s^* = \frac{\gamma_s^* P}{N_0 + \gamma_s^* N_z^*}. \quad (23)$$

Therefore, the capacity-distortion region in Theorem 1 can then be written as

$$\begin{aligned} R &= \mathbb{E}[\log_2(1 + \Gamma_c^*)] \\ &= \int_0^\infty \log_2 \left(1 + \frac{xP}{N_0 + xN_z^*}\right) f_{\gamma_c^*}(x) dx \end{aligned} \quad (24)$$

and

$$\begin{aligned} D_s &= \mathbb{E} \left[ \frac{\sigma_\theta^2}{1 + \Gamma_s^*} \right] \\ &= \int_0^\infty \frac{\sigma_\theta^2}{1 + \frac{xP}{N_0 + xN_z^*}} f_{\gamma_s^*}(x) dx, \end{aligned} \quad (25)$$

where  $f_{\gamma_c^*}(\cdot)$  is the probability density function (PDF) of the FAS selected gain obtained in [50], and  $f_{\gamma_s^*}(\cdot)$  is determined by the sensing side correlation model.

Equations (24) and (25) provide a direct bridge between the AI-limited ISAC framework and the existing FAS channel theory such that the AI bottleneck appears only through the additional noise variance  $N_z^*$ , while the finite- $L$  behavior and the influence of the length  $W$  enter through the FAS-selected gain distributions already characterized in [50].

## V. Asymptotic Behavior: FAS length, Spatial DoF, and AI Compensation

In this section, we analyze how the physical length of a fluid antenna influences the maximum gain extracted through port selection and how this, in turn, interacts with the AI-induced representation noise  $N_z^*$ . In contrast to selection schemes over i.i.d. fading, the selected port gain in an FAS is fundamentally limited by the spatial DoF of a 1D region of length  $W$ .

### A. Spatial DoF and Selected Port Gain Saturation

Under the Jakes correlation model, the communication channel vector  $\mathbf{h}_c = [h_{c,1}, \dots, h_{c,L}]^\top$  is complex Gaussian with Toeplitz covariance

$$R_{k,\ell}(W) = J_0\left(\frac{2\pi}{\lambda} \frac{W}{L-1} |k - \ell|\right). \quad (26)$$

As shown in [50], the high-SNR outage probability of the FAS-selected channel satisfies

$$\mathbb{P}(|h_{c,\text{FAS}}| < \Omega) = \frac{1}{\det(\mathbf{R})} \Omega^{2L'(W)} + o(\Omega^{2L'(W)}), \quad (27)$$

where  $L'(W)$  is the numerical rank of the correlation matrix  $\mathbf{R}$  and represents the effective number of spatial DoF supported by an FAS of length  $W$ . Consequently, the diversity order is given by  $D_{\text{FAS}}(W) \approx L'(W)$ , which is independent of the number of ports  $L$  once  $L$  is large enough. Thus, increasing  $L$  does not cause the selected port gain  $\gamma_c^* = \max_{\ell} |h_{c,\ell}|^2$  to diverge. Instead, as  $L \rightarrow \infty$  with fixed  $W$ ,  $\gamma_c^*$  converges in distribution to a length-limited random variable with finite mean and a finite upper tail determined by  $L'(W)$ . Hence, unlike the i.i.d. Rayleigh case where  $\gamma_c^*(L) = \Theta(\log L)$ , a 1D FAS exhibits length-limited gain scaling.

### B. Consequences for AI-Limited ISAC

Recall the effective SNR defined in (22), where the AI bottleneck introduces the ceiling

$$\Gamma_{\text{AI}} = \frac{P}{N_z^*} = 2^{C_{\text{AI}}} - 1. \quad (28)$$

If  $\gamma_c^*$  were unbounded, then  $\Gamma_c^* \rightarrow \Gamma_{\text{AI}}$ , allowing the system to fully achieve the AI-limited capacity-distortion bounds. But as  $\gamma_c^*$  saturates for fixed  $W$ , the effective SNR remains

strictly below this ceiling. Let  $\gamma_{c,\max}(W)$  be the maximum achievable selected port gain in the dense port limit. Then

$$\Gamma_c^*(W) \leq \frac{\gamma_{c,\max}(W)P}{N_0 + \gamma_{c,\max}(W)N_z^*}, \quad (29)$$

and the achievable communication rate satisfies

$$R(W) = \mathbb{E} [\log_2 (1 + \Gamma_c^*(W))] < C_{\text{AI}}. \quad (30)$$

Larger FAS length increases  $L'(W)$ , improves the upper tail of  $\gamma_c^*$ , and raises the effective SNR toward the AI ceiling. In the limiting case  $W \rightarrow \infty$ , the FAS supports an unbounded number of spatial DoF, so that the selected port gain can grow arbitrarily large under the adopted far-field fading model, and the effective SNR approaches the AI-imposed ceiling. These effects are now summarized by the following theorem.

**Theorem 2** (Length-Dependent Compensation of the AI Bottleneck). Let  $\gamma_c^*(W)$  denote the FAS-selected gain under Jakes correlated fading model. Then

- 1) For fixed FAS length  $W < \infty$ ,

$$R(W) < C_{\text{AI}} \quad (31)$$

and

$$D_s(W) > \frac{\sigma_\theta^2}{2^{C_{\text{AI}}}}. \quad (32)$$

- 2) If the FAS length increases such that  $\gamma_c^*(W) \rightarrow \infty$ , then the AI-limited ISAC bounds are achieved:

$$\lim_{W \rightarrow \infty} R(W) = C_{\text{AI}} \quad (33)$$

and

$$\lim_{W \rightarrow \infty} D_s(W) = \frac{\sigma_\theta^2}{2^{C_{\text{AI}}}}. \quad (34)$$

**Proof.** For fixed  $W$ , the selected port gain has a finite distribution determined by  $L'(W)$  [50]; thus  $\Gamma_c^*(W)$  remains strictly below the AI ceiling and the inequalities follow from monotone convergence and continuity of the logarithm. As  $W \rightarrow \infty$ , the numerical rank  $L'(W)$  grows without bound, the selected port gain diverges in probability, and the effective SNR converges to  $2^{C_{\text{AI}}} - 1$ , yielding the AI-limited expressions in Theorem 1, which completes the proof. ■

This result demonstrates that the FAS length, rather than the number of ports, governs the extent to which spatial diversity can mitigate the effects of the AI representation bottleneck.

## VI. VIB Encoder Design

The theoretical analysis in previous sections models the pre-channel AI mapping  $X \mapsto Z$  as a Gaussian channel that satisfies the information constraint  $I(X; Z) \leq C_{\text{AI}}$ . In this section, we describe a practical neural implementation of this mapping based on the VIB, which provides a parametric approximation to the optimal Gaussian encoder and can be trained directly from data. This section establishes how the theoretical bottleneck model can be realized in practice and how the resulting latent

representation approximates, and in the large-sample and optimal training limit recovers, the Gaussian structure used in our achievability proof.

### A. VIB Objective

The bottleneck is positioned before the physical channel, so the latent representation  $Z$  is generated from the ideal transmitted symbol  $X$  under the information constraint  $I(X; Z) \leq C_{\text{AI}}$ . The physical ISAC channel then operates on  $Z$ , producing the communication and sensing observations  $(Y_c, Y_s)$ . Accordingly, the dependency structure follows the Markov chain  $X \rightarrow Z \rightarrow (Y_c, Y_s)$ .

The VIB formulation approximates the constrained optimization  $I(X; Z) \leq C_{\text{AI}}$  via the Lagrangian

$$\mathcal{L}_{\text{VIB}} = \mathbb{E}_{p(x, m)} [\mathbb{E}_{p_\phi(z|x)} [-\log p_\psi(m|z)]] + \beta I_\phi(X; Z), \quad (35)$$

where  $\phi$  and  $\psi$  denote the encoder and decoder parameters, respectively, and  $\beta > 0$  controls the strength of the bottleneck. Larger  $\beta$  enforces a stricter compression and corresponds to a smaller effective AI capacity  $C_{\text{AI}}$ .

The MI term is approximated by the Kullback-Leibler (KL) divergence between the encoder and a prior as

$$I_\phi(X; Z) \approx \mathbb{E}_{p(x)} D_{\text{KL}}(p_\phi(z|x) \parallel p(z)), \quad (36)$$

where  $p(z)$  is typically chosen as a simple Gaussian prior. This approximation matches the theoretical Gaussian channel used in Section III and ensures that the learned latent representation  $Z$  approximates the optimal Gaussian solution for the information-constrained encoder.

### B. Gaussian Reparameterization

To align the neural encoder with the optimal channel structure, we model

$$p_\phi(z|x) = \mathcal{CN}(\mu_\phi(x), \Sigma_\phi(x)), \quad (37)$$

and using the standard reparameterization technique, we write

$$z = \mu_\phi(x) + \Sigma_\phi^{1/2}(x) \epsilon, \text{ with } \epsilon \sim \mathcal{CN}(0, I), \quad (38)$$

which allows low-variance gradient estimation.

Choosing the prior as  $p(z) = \mathcal{CN}(0, \sigma_z^2 I)$  yields the KL term as

$$\begin{aligned} D_{\text{KL}} &= \log \frac{|\sigma_z^2 I|}{|\Sigma_\phi(x)|} + \text{tr}((\sigma_z^2 I)^{-1} \Sigma_\phi(x)) \\ &\quad + \mu_\phi(x)^\dagger (\sigma_z^2 I)^{-1} \mu_\phi(x) - d. \end{aligned} \quad (39)$$

Note that minimizing (35) with respect to  $(\phi, \psi)$  encourages  $\Sigma_\phi$  to approach a constant isotropic covariance, so the effective learned bottleneck approximates the form  $Z = X + W_z$  with  $W_z \sim \mathcal{CN}(0, N_z I)$ , which is exactly the Gaussian structure required by Theorem 1. Also, the trained variance  $N_z$  satisfies

$$I(X; Z) \approx C_{\text{AI}}, \quad (40)$$

such that  $N_z$  approaches the theoretical optimum  $N_z^* = P/(2^{C_{\text{AI}}} - 1)$ , which comes from (28).

Algorithm 1 VIB Training for the AI-limited FAS-aided ISAC Encoder

- 1: Initialize encoder parameters  $\phi$  and decoder parameters  $\psi$ .
- 2: for each training minibatch do
- 3: Sample symbols  $x$  and corresponding messages  $m$ .
- 4: Compute encoder statistics  $\mu_\phi(x)$  and  $\Sigma_\phi(x)$ .
- 5: Sample  $z$  via the reparameterization (38).
- 6: Evaluate reconstruction loss  $\text{CE}(m, \psi(z))$ .
- 7: Compute KL divergence using (39).
- 8: Form total VIB loss  $\mathcal{L}_{\text{VIB}} = \text{CE}(m, \psi(z)) + \beta D_{\text{KL}}$ .
- 9: Update  $(\phi, \psi)$  using stochastic gradient descent.
- 10: end for

TABLE II  
Simulation parameters.

Quantity	Symbol	Value
Transmit power	$P$	30dBm
Noise variances	$N_0$	0.1
Sensing parameter variance	$\sigma_\theta^2$	1
Wavelength	$\lambda$	1 (normalized)
Number of ports	$L$	256
MIMO	$(N_t, N_r)$	(2, 2)
Length of fluid antenna	$W$	$\{0.5\lambda, 2\lambda, 8\lambda\}$
AI-capacity set for frontier	$C_{\text{AI}}$	$\{2, 4, 6, \infty\}$

### C. Training Algorithm

Algorithm 1 summarizes the learning process. The neural encoder receives input symbols  $x$  and produces the latent  $z$ . The decoder  $p_\psi(m|z)$  performs message reconstruction during training, ensuring that  $Z$  retains the information needed for communication decoding. Because  $Z$  is fed into the physical ISAC model, the learned latent representations are directly compatible with the AI-limited FAS-aided ISAC system. The term  $\text{CE}(m, \psi(z))$  denotes the standard cross-entropy (CE) loss between the true message label  $m$  and the decoder output distribution  $\psi(z)$ , namely  $\text{CE}(m, \psi(z)) = -\log p_\psi(m|z)$ .

By tuning  $\beta$  such that  $I_\phi(X; Z) \approx C_{\text{AI}}$ , the learned encoder approximates to a Gaussian bottleneck whose latent variance approaches the equivalent representation noise  $N_z^*$  used in the theoretical development. Thus, the VIB framework provides a principled and practical realization of an encoder that closely matches the optimal encoder for the AI-limited FAS-enabled ISAC architecture.

## VII. Numerical Results

Here, we present numerical results to validate the theoretical analysis and illustrate the impact of the AI representation bottleneck and FAS on ISAC performance. The simulation parameters are summarized in Table II, including the transmit power, noise variance, AI-capacity budget, and FAS configuration. Benchmarks such as single-input single-output (SISO) and MIMO systems are compared with the proposed FAS-enabled ISAC receiver with different physical lengths.

Fig. 2 illustrates the achievable communication rate  $R$  as a function of the AI-capacity budget  $C_{\text{AI}}$  for several

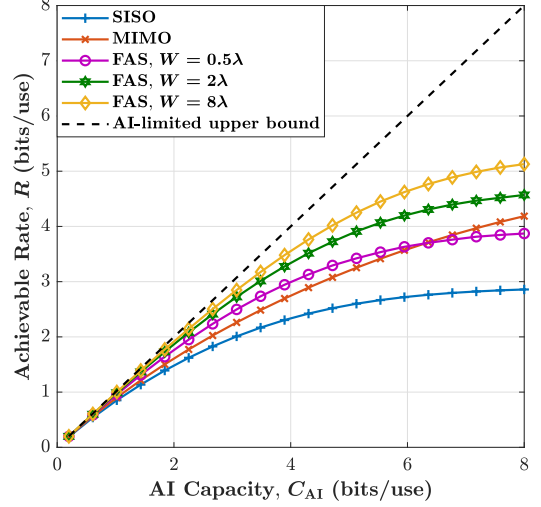


Fig. 2. Achievable communication rate  $R$  versus AI-capacity  $C_{\text{AI}}$ .

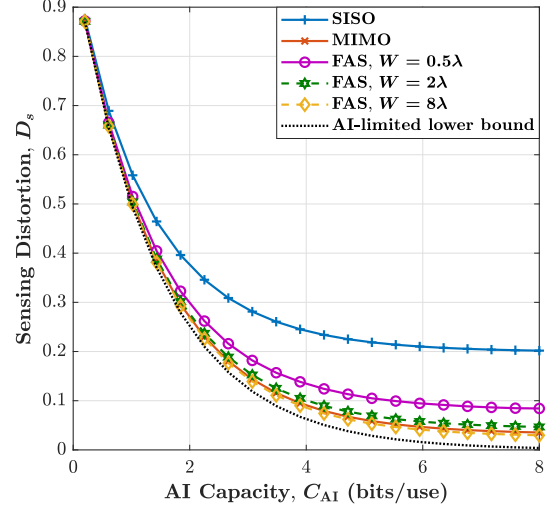


Fig. 3. Sensing distortion  $D_s$  versus AI-capacity  $C_{\text{AI}}$ .

representative architectures, including classical SISO and MIMO links as well as the proposed FAS-based ISAC receiver with different antenna length. Across all configurations, the achievable rate increases monotonically with  $C_{\text{AI}}$ , reflecting the fact that a larger learning-capacity budget reduces the amount of information lost through the AI bottleneck and thereby enables more accurate preservation of channel-relevant features. We can also see that the SISO case exhibits the lowest achievable rate over the full range of  $C_{\text{AI}}$ , since the effective SNR remains strictly limited by a single-antenna channel gain. The  $2 \times 2$  MIMO configuration provides a substantial improvement due to spatial multiplexing, and its rate approaches the AI-limited upper bound  $R = C_{\text{AI}}$  more closely than the SISO case.

The FAS curves reveal that increasing  $W$  directly enhances the rate under the same learning-capacity con-

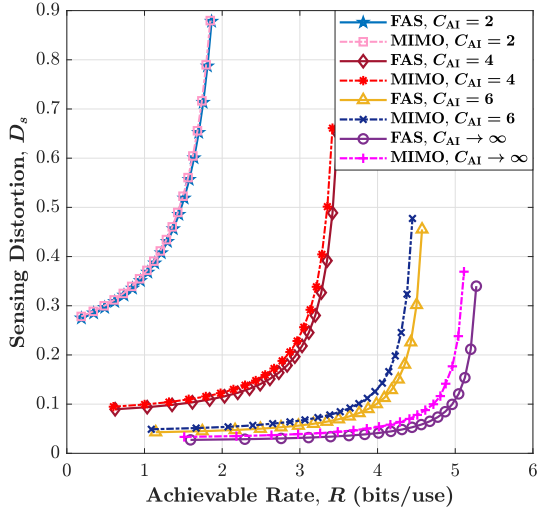


Fig. 4. Joint rate-sensing trade-off for the proposed model when  $W = 8\lambda$ .

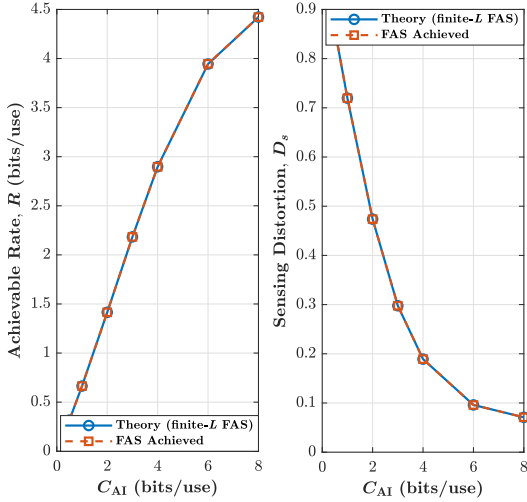


Fig. 5. Validation of theoretical and achieved performance.

straint. A small FAS of  $W = 0.5\lambda$  provides only modest gains over conventional MIMO, but as the length expands to  $W = 8\lambda$ , the resulting spatial diversity and angular resolution significantly boost the effective channel gain distribution. Consequently, larger FAS lengths yield markedly higher rates and approach the AI-limited bound more rapidly. This behavior confirms the benefit of dense spatial sampling when the AI encoder compresses the ideal transmit symbol into a low-capacity latent representation, namely, richer spatial observability mitigates the information loss caused by the finite  $C_{AI}$ . Furthermore, as  $C_{AI}$  increases, the gain of larger FAS becomes increasingly pronounced, highlighting that the combination of extended spatial length and a sufficiently expressive AI module produces the highest throughput among the examined architectures.

Fig. 3 presents the sensing distortion  $D_s$  in terms of

the AI-capacity  $C_{AI}$  for several receiver architectures, including SISO,  $2 \times 2$  MIMO, and FAS with different lengths. Across all curves, we see that the sensing distortion decreases monotonically with the available AI-capacity. This behavior reflects the fact that a larger information budget allows the AI module to retain a more faithful latent representation of the ideal transmit symbol, which in turn improves the quality of the received sensing observations.

At small AI capacities, i.e., below approximately 2 bits/use, all architectures operate in a highly compressed regime in which the learning bottleneck dominates system performance. In this region, the distortion values are relatively high because the latent representation cannot preserve the fine-grained structure of the transmitted waveform that interacts with the propagation environment. Even under these tight constraints, the FAS architectures already provide noticeable improvement over SISO and conventional MIMO reception due to their ability to capture richer spatial structure. As  $C_{AI}$  increases, the differences between architectures become more pronounced. The  $2 \times 2$  MIMO system achieves significantly lower distortion than the SISO case, owing to its larger effective sensing gain. The FAS configurations further enhances performance, and their relative advantage grows with its physical length. A small length ( $W = 0.5\lambda$ ) already delivers meaningful gains, while medium and large lengths ( $W = 2\lambda$ ) and ( $W = 8\lambda$ ) achieve substantially lower distortion by exploiting their increased spatial resolution and diversity. Additionally, we observe that for moderate and large AI capacities, the benefit of larger FAS lengths becomes increasingly pronounced even though port selection is communication-based, highlighting that richer spatial sampling mitigates the information loss caused by the finite. The theoretical AI-limited lower bound, shown as a dotted curve, represents the minimum distortion achievable when the learning representation incurs no additional information loss. Larger FAS lengths approach this bound more closely, showing their ability to fully exploit the available AI-capacity and preserve nearly all relevant sensing information.

Fig. 4 depicts the joint relationship between the communication rate  $R$  and the sensing distortion  $D_s$  for the proposed AI-constrained ISAC architecture when the FAS is configured with a length of  $W = 8\lambda$ . It is observed that for the smallest AI-capacity  $C_{AI} = 2$  bits/use, both architectures operate in a strongly learning-limited regime. The equivalent AI noise remains large, so only a coarse latent representation of the ideal transmit symbol can be preserved. As a result, the achievable rates are modest, roughly below 1.5 bits/use, and the sensing distortion remains relatively high over the entire frontier, with  $D_s$  approaching values close to unity when the operating point is pushed toward maximum rate. In this regime, the difference between FAS and conventional MIMO is noticeable but not dramatic, since the AI bottleneck dominates any advantage provided by additional spatial structure.

When the AI-capacity increases to  $C_{\text{AI}} = 4$  bits/use, the effective AI noise is significantly reduced and both rate and sensing performance improve. The frontiers shift downwards and to the right, indicating simultaneously lower distortion and higher rate. Here, the benefit of the FAS becomes clearer such that for the same target distortion, the FAS curve supports a larger rate than the MIMO benchmark, and for a fixed rate the FAS achieves a smaller distortion. This gain comes from the richer spatial sampling offered by the dense FAS ports, more effectively shapes the distribution of the selected port gains, allowing the AI module can encode the most informative spatial modes within its finite capacity budget.

The trend continues as the AI-capacity is further increased to  $C_{\text{AI}} = 6$  bits/use. The frontiers expand substantially, with FAS rates exceeding 4 bits/use while maintaining distortions well below 0.1 over a wide range of operating points. In contrast, the MIMO curve is consistently contained within the FAS region, confirming that FAS can exploit the additional AI bits more efficiently. Intuitively, once the AI bottleneck becomes less severe, the system performance is increasingly dictated by the physical channel gains. The large-length FAS offers both higher effective communication SNR and stronger sensing gain than the fixed-array MIMO baseline, and this advantage is directly reflected in the rate-distortion frontier.

The curves labeled  $C_{\text{AI}} \rightarrow \infty$  correspond to the idealized case in which the learning module has effectively unbounded capacity and introduces no additional representation noise. These frontiers characterize the fundamental joint performance dictated solely by the physical channel and noise statistics. Even in this ideal case, FAS continues to dominate the  $2 \times 2$  MIMO system, achieving the lowest sensing distortion for a given rate and the highest rate for a given distortion. Comparing the finite  $C_{\text{AI}}$  curves with their  $C_{\text{AI}} \rightarrow \infty$  counterparts reveals a clear saturation behavior such that increasing the AI-capacity beyond approximately 6 bits/use yields only marginal improvements, since the system is then limited mainly by thermal noise rather than by the learning bottleneck.

Finally, Fig. 5 shows the validation of the proposed finite- $L$  FAS performance characterization under the Jakes' spatial correlation model. This figure compares the communication rate and sensing distortion predicted by the finite- $L$  theory, obtained by evaluating (16)–(17) using the exact distribution of the selected port gain  $\gamma_c^*$ , with Monte Carlo simulations of a practical FAS with  $L = 256$  ports. The theoretical and simulated curves coincide across the entire range of AI capacities  $C_{\text{AI}}$ , confirming that the analytical model accurately captures the behavior of spatially correlated FAS arrays. This close agreement verifies that the representation-noise interpretation of the AI bottleneck remains valid under realistic correlation structures and that the proposed finite- $L$  analysis provides an accurate prediction of the achievable ISAC performance.

## VIII. Conclusion

This work presented the first information-theoretic characterization of FAS-assisted ISAC under a pre-channel AI representation bottleneck. By modeling the AI encoder as an information-constrained mapping and the FAS as a spatially correlated port selection architecture, we derived the capacity-distortion region in closed form and established matching converse and achievability bounds. The analysis revealed that the AI bottleneck appears as an equivalent representation noise that uniformly degrades both communication and sensing SNRs at the selected port. For FAS, we further quantified the behavior of the selected port gain and showed that its growth with the physical length of the array is sufficient to offset the information loss induced by the AI constraint. As a result, both the achievable communication rate and sensing MSE approach their AI-limited fundamental limits as the fluid antenna length increases. Our numerical results suggest that FAS can act as an effective spatial amplifier for AI-limited transceivers, enabling ISAC systems to recover much of the performance otherwise lost due to finite representation capability.

## References

- [1] J. A. Zhang et al., “An overview of signal processing techniques for joint communication and radar sensing,” *J. Sel. Topics Signal Process.*, vol. 15, no. 6, pp. 1295–1315, Nov. 2021.
- [2] F. Liu et al., “Seventy years of radar and communications: The road from separation to integration,” *IEEE Signal Process. Mag.*, vol. 40, no. 5, pp. 106–121, Jul. 2023.
- [3] F. Rostami Ghadi, F. J. López Martínez, K. K. Wong, and C. Masouros, “Information-theoretic limits of integrated sensing and communication with finite learning capacity”, arXiv preprint, [arXiv:2512.13292v1](https://arxiv.org/abs/2512.13292v1), 2025.
- [4] K. K. Wong, A. Shojaeifard, K.-F. Tong, and Y. Zhang, “Fluid antenna systems,” *IEEE Trans. Wireless Commun.*, vol. 20, no. 3, pp. 1950–1962, Mar. 2021.
- [5] W. K. New et al., “A tutorial on fluid antenna system for 6G networks: Encompassing communication theory, optimization methods and hardware designs,” *IEEE Commun. Surv. Tuts.*, vol. 27, no. 4, pp. 2325–2377, Aug. 2025.
- [6] H. Hong et al., “A contemporary survey on fluid antenna systems: Fundamentals and networking perspectives,” *IEEE Trans. Netw. Sci. Eng.*, vol. 13, pp. 2305–2328, 2026.
- [7] W. K. New et al., “Fluid antenna systems: Redefining reconfigurable wireless communications,” *IEEE J. Sel. Areas Commun.*, DOI:10.1109/JSAC.2025.3632097, 2026.
- [8] T. Wu et al., “Fluid antenna systems enabling 6G: Principles, applications, and research directions,” to appear in *IEEE Wireless Commun.*, DOI:10.1109/MWC.2025.3629597, 2025.
- [9] W.-J. Lu et al., “Fluid antennas: Reshaping intrinsic properties for flexible radiation characteristics in intelligent wireless networks,” *IEEE Commun. Mag.*, vol. 63, no. 5, pp. 40–45, May 2025.
- [10] L. Zhu and K. K. Wong, “Historical review of fluid antenna and movable antenna,” arXiv preprint, [arXiv:2401.02362](https://arxiv.org/abs/2401.02362), 2024.
- [11] Y. Shen et al., “Design and implementation of mmWave surface wave enabled fluid antennas and experimental results for fluid antenna multiple access,” to appear in *IEEE Antennas & Wireless Propag. Lett.*, DOI:10.1109/LAWP.2026.3657059, 2026.
- [12] R. Wang et al., “Electromagnetically reconfigurable fluid antenna system for wireless communications: Design, modeling, algorithm, fabrication, and experiment,” *IEEE J. Select. Areas Commun.*, DOI:10.1109/JSAC.2025.3625163, 2026.
- [13] S. Zhang et al., “Fluid antenna systems enabled by reconfigurable holographic surfaces: Beamforming design and experimental validation,” *IEEE J. Select. Areas Commun.*, DOI:10.1109/JSAC.2025.3618797, 2026.

[14] B. Liu, K.-F. Tong, K. K. Wong, C.-B. Chae, and H. Wong, "Programmable meta-fluid antenna for spatial multiplexing in fast fluctuating radio channels," *Optics Express*, vol. 33, no. 13, pp. 28898–28915, 2025.

[15] B. Liu et al., "Meta fluid antenna: Architecture design, performance analysis, experimental examination," arXiv preprint, [arXiv:2509.12032](https://arxiv.org/abs/2509.12032), Sept. 2025.

[16] J. Zhang et al., "A novel pixel-based reconfigurable antenna applied in fluid antenna systems with high switching speed," *IEEE Open J. Antennas & Propag.*, vol. 6, no. 1, pp. 212–228, Feb. 2025.

[17] B. Liu, T. Wu, K. K. Wong, H. Wong, and K. F. Tong, "Wideband pixel-based fluid antenna system: An antenna design for smart city," *IEEE Internet Things J.*, DOI:10.1109/JIOT.2025.3637319, 2025.

[18] K. K. Wong, C. Wang, S. Shen, C.-B. Chae and R. Murch, "Reconfigurable pixel antennas meet fluid antenna systems: A paradigm shift to electromagnetic signal and information processing," *IEEE Wireless Commun.*, DOI:10.1109/MWC.2025.3625130, 2026.

[19] K.-F. Tong, B. Liu, and K. K. Wong, "Designs and challenges in fluid antenna system hardware," *Electronics*, vol. 14, no. 7, p. 1458, 2025.

[20] C. Wang et al., "Fluid antenna system liberating multiuser MIMO for ISAC via deep reinforcement learning," *IEEE Trans. Wireless Commun.*, vol. 23, no. 9, pp. 10879–10894, Sept. 2024.

[21] F. R. Ghadi, K. K. Wong, F. Javier López-Martínez, H. Shin and L. Hanzo, "Performance analysis of FAS-aided NOMA-ISAC: A backscattering scenario," *IEEE Internet Things J.*, vol. 12, no. 23, pp. 51326–51340, Dec. 2025.

[22] J. Zou et al., "Shifting the ISAC trade-off with fluid antenna systems," *IEEE Wireless Commun. Lett.*, vol. 13, no. 12, pp. 3479–3483, Dec. 2024.

[23] L. Zhou, J. Yao, M. Jin, T. Wu and K. K. Wong, "Fluid antenna-assisted ISAC systems," *IEEE Wireless Commun. Lett.*, vol. 13, no. 12, pp. 3533–3537, Dec. 2024.

[24] B. Tang et al., "Full-duplex FAS-assisted base station for ISAC," *IEEE Trans. Wireless Commun.*, vol. 25, pp. 2922–2938, 2025.

[25] M. Ahmadipour, M. Kobayashi, M. Wigger and G. Caire, "An information-theoretic approach to joint sensing and communication," *IEEE Trans. Inf. Theory*, vol. 70, no. 2, pp. 1124–1146, Feb. 2024.

[26] M. Ahmadipour and M. Wigger, "An information-theoretic approach to collaborative integrated sensing and communication for two-transmitter systems," *IEEE J. Sel. Areas Inf. Theory*, vol. 4, pp. 112–127, 2023.

[27] H. Nikbakht, M. Wigger, S. Shamai and H. V. Poor, "Integrated sensing and communication in the finite blocklength regime," in Proc. IEEE Int. Symp. Inf. Theory (ISIT), pp. 2790–2795, 7-12 Jul. 2024, Athens, Greece.

[28] H. Joudeh and G. Caire, "Joint communication and state sensing under logarithmic loss," in Proc. IEEE Int. Symp. Joint Commun. & Sensing (JC&S), 19-21 Mar. 2024, Leuven, Belgium.

[29] H. Hua, T. X. Han and J. Xu, "MIMO integrated sensing and communication: CRB-rate tradeoff," *IEEE Trans. Wireless Commun.*, vol. 23, no. 4, pp. 2839–2854, Apr. 2024.

[30] J. An, H. Li, D. W. K. Ng and C. Yuen, "Fundamental detection probability vs. achievable rate tradeoff in integrated sensing and communication systems," *IEEE Trans. Wireless Commun.*, vol. 22, no. 12, pp. 9835–9853, Dec. 2023.

[31] Z. Ren et al., "Fundamental CRB-rate tradeoff in multi-antenna ISAC systems with information multicasting and multi-target sensing," *IEEE Trans. Wireless Commun.*, vol. 23, no. 4, pp. 3870–3885, Apr. 2024.

[32] S. Aldirmaz-Colak et al., "A comprehensive review on ISAC for 6G: Enabling technologies, security, and AI/ML perspectives," *IEEE Access*, vol. 13, pp. 97152–97193, 2025.

[33] J. Zhang et al., "Intelligent integrated sensing and communication: A survey," *Sci. China Inf. Sci.*, vol. 63, no. 3, 131301, 2025.

[34] X. Liu, H. Zhang, K. Sun, K. Long and G. K. Karagiannidis, "AI-driven integration of sensing and communication in the 6G era," *IEEE Netw.*, vol. 38, no. 3, pp. 210–217, May 2024.

[35] M. Vaezi, GA Baduge, E. Ollila, and SA Vorobyov, "AI-empowered integrated sensing and communications," arXiv preprint, [arXiv:2504.13363v1](https://arxiv.org/abs/2504.13363v1). 2025.

[36] N. Tishby, F. C. Pereira, and W. Bialek, "The information bottleneck method," arXiv preprint, [arXiv:physics/0004057v1](https://arxiv.org/abs/physics/0004057v1), 2000.

[37] A. A. Alemi, I. Fischer, J. V. Dillon, and K. Murphy, "Deep variational information bottleneck," arXiv preprint, [arXiv:1612.00410v7](https://arxiv.org/abs/1612.00410v7), 2016.

[38] N. Shlezinger and Y. C. Eldar, "Deep task-based quantization," *Entropy*, vol. 23, no. 1, 104, 2021.

[39] F. Xi, N. Shlezinger and Y. C. Eldar, "BiLiMO: Bit-limited MIMO radar via task-based quantization," *IEEE Trans. Sig. Process.*, vol. 69, pp. 6267–6282, 2021.

[40] W. K. New, K. K. Wong, H. Xu, K. F. Tong, and C.-B. Chae, "An information-theoretic characterization of MIMO-FAS: Optimization, diversity-multiplexing tradeoff and  $q$ -outage capacity," *IEEE Trans. Wireless Commun.*, vol. 23, no. 6, pp. 5541–5556, Jun. 2024.

[41] F. Rostami Ghadi et al., "Fluid antenna-assisted dirty multiple access channels over composite fading," *IEEE Commun. Lett.*, vol. 28, no. 2, pp. 382–386, Feb. 2024.

[42] F. R. Ghadi et al., "Fluid antenna multiple access with simultaneous non-unique decoding in strong interference channel," *IEEE Trans. Wireless Commun.*, vol. 24, no. 12, pp. 10183–10195, Dec. 2025.

[43] C. Wang et al., "AI-empowered fluid antenna systems: Opportunities, challenges, and future directions," *IEEE Wireless Commun.*, vol. 31, no. 5, pp. 34–41, Oct. 2024.

[44] N. Waqar, K. K. Wong, K.-F. Tong, A. Sharples and Y. Zhang, "Deep learning enabled slow fluid antenna multiple access," *IEEE Commun. Lett.*, vol. 27, no. 3, pp. 861–865, Mar. 2023.

[45] Z. Chai, K. K. Wong, K.-F. Tong, Y. Chen and Y. Zhang, "Port selection for fluid antenna systems," *IEEE Commun. Lett.*, vol. 26, no. 5, pp. 1180–1184, May 2022.

[46] N. Waqar et al., "Opportunistic fluid antenna multiple access via team-inspired reinforcement learning," *IEEE Trans. Wireless Commun.*, vol. 23, no. 9, pp. 12068–12083, Sept. 2024.

[47] H. Jiang, Z. Wang, Y. Liu and A. Nallanathan, "Beam alignment for MIMO fluid antenna systems: An online-learning approach," in Proc. IEEE/CIC Int. Conf. Commun. China (ICCC), 10-13 Aug. 2025, Shanghai, China.

[48] N. Tishby, F. C. Pereira, and W. Bialek, "The information bottleneck method," arXiv preprint, [arXiv:physics/0004057v1](https://arxiv.org/abs/physics/0004057v1), 2000.

[49] A. A. Alemi, I. Fischer, J. V. Dillon, and K. Murphy, "Deep variational information bottleneck," arXiv preprint, [arXiv:1612.00410v7](https://arxiv.org/abs/1612.00410v7), 2016.

[50] W. K. New, K. K. Wong, H. Xu, K.-F. Tong and C.-B. Chae, "Fluid antenna system: New insights on outage probability and diversity gain," *IEEE Trans. Wireless Commun.*, vol. 23, no. 1, pp. 128–140, Jan. 2024.